RSC Advances

PAPER

View Article Online
View Journal | View Issue

Cite this: *RSC Adv.*, 2025, **15**, 8764

A facile and green one-step synthesis of Ag/reduced graphene oxide and its application in catalysts and SERS†

Yanling Jia [a] and Ke Zhang *[bc]

Herein, we present a facile one-step approach for synthesizing Ag/reduced graphene oxide (Ag–rGO) through synchronous reduction and *in situ* coagulation of graphene oxide (GO) and silver nitrate ($AgNO_3$) under a nitrogen atmosphere. In this process, GO serves as the carrier and template, $AgNO_3$ as the precursor, and rutin functions both as the reducing and stabilizing agent. The Ag–rGO nanocomposite is synthesized using an eco-friendly method, where spherical silver nanoparticles are randomly dispersed on the surface of reduced graphene oxide (rGO). This nanocomposite exhibits excellent catalytic activity for degrading methylene blue (MB) and demonstrates good surface-enhanced Raman scattering (SERS) activity as a SERS substrate. It was found that 3 mg Ag–rGO attained a decolorization rate of 96% within merely 9 minutes, with a corresponding reaction rate constant (k) of 0.362 min^{-1}. SERS detection of R6G also exhibited good performance in terms of detection limits in the order of 10^{-7} M, an enhancement factor of 3.03×10^5, and high reproducibility (the maximum intensity deviation < 7.01%). The excellent performance can be attributed to the decreased size of Ag on the nanocomposite and the larger specific surface area achieved through the *in situ* synchronous reduction and coagulation method. Additionally, the *in situ* enrichment effect and superior electron transfer efficiency further enhance the catalytic performance of the nanocomposite, and the synergistic effect of chemical enhancement and electromagnetic enhancement contribute to the good Raman enhancement effect. The effects of reaction parameters such as time and varying reactant ratios on the catalytic and SERS activities of the nanocomposite were also investigated. These findings indicate the potential ability of the Ag–rGO for practical environmental monitoring and treatment applications.

Received 1st January 2025
Accepted 18th March 2025

DOI: 10.1039/d5ra00001g

rsc.li/rsc-advances

1 Introduction

While organic dyes can infuse our daily lives with vibrancy, they seriously threaten the ecological environment and human health.[1] Aquatic contamination emerges as one of the most pressing challenges of the twenty-first century.[2,3] Advancing green chemistry at the source and exploring effective methods for dye wastewater treatment to meet safe discharge standards and promote resource utilization is essential for achieving Sustainable Development Goals. Dye removal methods primarily include adsorption and catalytic degradation.[4–7] The linchpin of the adsorption method is the adsorbent, which typically includes activated carbon, ion exchange resin, silica gel, diatomaceous earth,[8–11] *etc.* However, these traditional adsorbents suffer from limitations such as slow processing rates, challenges in degradation, and susceptibility to secondary pollution.[12,13] New adsorbents have recently emerged to address these challenges, including natural polymers,[14] nanocarbon materials,[15–17] and magnetic,[18] and composite adsorbents,[19–21] which offer higher efficiency and faster adsorption rates. Notably, nanocarbon adsorbents provide a high specific surface area and rapid adsorption. Additionally, transforming toxic organic pollutants into less harmful, reusable substances is an effective and sustainable treatment approach. Noble metal nanostructures[22] have shown potential as catalysts for degrading pollutants under mild conditions, facilitating the resource utilization of wastewater; however, their practical application is hindered by high surface energy and poor thermodynamic stability.[23]

Graphene has broad prospects for applications in catalytic support due to its unique two-dimensional (2D) characteristic structure, large surface area, well-developed porosity, outstanding electronic properties, and promising mechanical and thermal stability.[24–26] Loading noble metals on graphene is not only expected to solve the disadvantages of high surface

[a]*College of Advanced Materials Engineering, Jiaxing Nanhu University, Jiaxing 314000, China*

[b]*Beijing Institute of Technology, Beijing 100081, China. E-mail: cr7zhangke@outlook.com*

[c]*Yangtze Delta Region Academy of Beijing Institute of Technolog, Jiaxing 314000, PR China*

† Electronic supplementary information (ESI) available. See DOI: https://doi.org/10.1039/d5ra00001g

energy and poor thermodynamic stability of noble metals but also exhibits superior comprehensive properties. For instance, Li *et al.*[27] have successfully synthesized Ag nanoclusters (~3.57 nm) directly on reduced graphene oxide (rGO). The resulting nanocomposites exhibit high catalytic activity for the reduction of 4-nitrophenol(4-NP). Additionally, these nanocomposites have been proven to be efficient antibacterial agents and photothermal ablation agents. Yang and co-workers[28] have demonstrated a preparation method of AuNPs/rGO nanocomposite films by a one-step dual reduction of graphene oxide and chloroauric acid using argon plasma, the nanocomposites can successfully catalyze the reduction of toxic 4-NP into non-toxic 4-aminophenol (4-AP). Although the aforementioned studies are inconsistent with the specific applications investigated in this work or face challenges in achieving scalable batch production or high energy consumption, we acknowledge the critical importance of developing one-step synthesis methodologies and promoting the significant application of graphene-supported noble metal nanocomposites.

Therefore, we have demonstrated a facile and green one-step route of synchronous reduction and *in situ* coagulation for preparing Ag/reduced graphene oxide in this work. GO and $AgNO_3$ were used as support and precursor, respectively. Under the reducing and stabilizing effect of the natural product rutin, and with the synchronous reduction reaction of $AgNO_3$ and GO serving as the triggering condition, bidirectional aggregation and *in situ* composition of nano metals and graphene were achieved, yielding Ag–rGO nanocomposites. This approach circumvents tedious steps such as the separate reduction process and the subsequent loading. The reagents used are also non-toxic and can achieve large-scale production. Moreover, the size of Ag nanoparticles loaded in Ag–rGO nanocomposites is smaller than that of individual Ag nanoparticles, resulting in a larger specific surface area for the nanocomposite and high catalytic efficiency.[29] Surprisingly, the as-prepared Ag–rGO not only serves as an excellent catalyst for the reduction of methylene blue (MB) due to its *in situ* enrichment and superior electron transfer efficiency[30] but also functions as an efficient SERS substrate due to the combination of Ag's typical electromagnetic enhancement effect, graphene's chemical enhancement effect, quenching of molecular fluorescence, and high adsorption capacity for target molecules.[31,32] Meanwhile, this work provides a facile and general one-step approach for modifying metal nanoparticles on the surface of rGO for use as a nanocatalyst and SERS substrate. The results involved have been discussed in detail in the following part.

2 Materials and methods

2.1. Materials

Graphite powders with a mesh size of 325 and a purity of 99.9995% were sourced from Alfa Aesar Co. Ltd. Concentrated sulfuric acid (H_2SO_4, 98%), concentrated phosphoric acid (H_3PO_4, 85%), potassium permanganate ($KMnO_4$, 99.5%), hydrogen peroxide (H_2O_2, 30%) and silver nitrate ($AgNO_3$, 99.8%), fluorescent dyes such as rhodamine 6G (R6G, 99%) and methylene blue (MB, 98%) were all purchased from Beijing Chemicals Co. Ltd. Rutin hydrate (Rutin, 98%) was purchased from Macklin Biochemical Company in Shanghai. Sodium borohydride (98%) was purchased from Sinopharm Chemical Reagent Co., Ltd. The silicon wafers were purchased from ZhongNuo Advanced Material (Beijing) Technology Co., Ltd. The Dialysis bag(MD44-3500) was purchased by Beijing Solaibao Technology Co., Ltd. The Microporous PES membrane (mixed fiber water system, 0.22 μm pore size) was purchased from Sinopharm Chemical Reagent Co., Ltd. In all cases, deionized water was used to prepare the solution.

2.2. Preparation of GO

GO was prepared from natural graphite powders using the improved Hummers' method. Briefly, the process commenced with the oxidation of graphite powders using a mixture of concentrated sulfuric acid (H_2SO_4), concentrated phosphoric acid (H_3PO_4), and potassium permanganate ($KMnO_4$). Subsequently, the resultant product underwent treatment with hydrogen peroxide (H_2O_2), followed by a series of water washing and tip sonication steps to ensure thorough purification and sufficient exfoliation. The detailed procedure can be found in the ref. 26 and 33.

2.3. Preparation of Ag–rGO

The preparation procedure for Ag–rGO is described as follows: start by taking 1250 g of GO dispersion (2 mg g^{-1}). Adjust the pH of dispersion to 12 by adding an appropriate volume of ammonia solution under stirring. Subsequently, introduce 2.5 g of $AgNO_3$ and 10 g of rutin into the dispersion while stirring in a nitrogen-enriched environment at 35 °C until complete dissolution. The mixture is further heated at 95 °C within 30 minutes, continuously stirred, and supplied with nitrogen gas, continuous reaction for 12 hours, obtaining a brown dispersion. Post-processing involves dialysis of the brown dispersion for two weeks, followed by freeze-drying to yield a powdered solid product, designated as Ag–rGO. To enhance the synthesis process, we investigated the impact of reaction time and rutin quantities, with detailed formulations outlined in Table S1.† Furthermore, experiments were conducted using varying amounts of GO and $AgNO_3$, with the resulting products designated as Ag–rGO-*x*-*y*, where *x* and *y* represent the mass ratio of $AgNO_3$ (*x*) to GO (*y*) during the preparation process. Unless stated otherwise, Ag–rGO refers specifically to Ag–rGO-5-5.

Comparatively, Ag nanoparticles were prepared using a similar process but without additional GO. R–rGO was prepared using a similar process but without additional $AgNO_3$.

2.4. Calculation of bandgap

The bandgap of GO and Ag–rGO samples were calculated and analyzed according to Tauc formula:[34]

$$\alpha(h\nu) = C(h\nu - E_g)^n \quad (1)$$

where C denotes a constant, while α, $h\nu$, and E_g correspond to the absorption coefficient, and photon energy, and represents bandgap width, respectively. The parameter n is pivotal in

distinguishing between direct and indirect bandgap materials; it is assigned a value of 0.5 for materials with a direct bandgap, and 2 for those with an indirect bandgap.

2.5. Catalytic reduction of MB

In a typical procedure for the catalytic reduction of MB by $NaBH_4$, a specific mass of Ag–rGO powder was dispersed into 50 mL of MB dye aqueous solution (100 mg L^{-1}) under stirring for 10 min, and then rapidly injected 0.5 mL of $NaBH_4$ aqueous solution (3×10^{-5} mg L^{-1}) into the above solution. Aliquots are collected at predetermined time intervals and filtered through a 0.22 μm PES membrane to yield a clear supernatant. The absorbance at 622 nm, identified as the characteristic peak in UV-vis spectrophotometry, is utilized to evaluate the catalytic performance of Ag–rGO. According to Lambert Beer's law, the variation in MB concentration within the solution is calculated, facilitating the analysis of the catalytic reaction kinetics. The formula for the decolorization rate of methylene blue is as follows:

$$\text{Decolorization rate} = \frac{A_0 - A}{A_0} \times 100\% \quad (2)$$

where A_0 denotes the initial absorbance of the MB solution, whereas A signifies the absorbance of the MB solution at a specified time point.

The kinetic equation for the MB reduction reaction is:

$$-\frac{dc}{dt} = kc^{\alpha} \quad (3)$$

where c represents the concentration of MB solution at various reaction times, t indicates the elapsed reaction time, k is the reaction rate constant, and α represents the order of the reaction. By plotting $\ln(c_t/c_0)$ against the reaction time t, the kinetics of the MB reduction reaction can be investigated.

2.6. SERS experiments

In the SERS experiments, R6G was employed as the probe molecule. The adsorption of R6G onto the surfaces of the Ag–rGO nanocomposites was facilitated through a soaking process. The SERS-active substrate was fabricated by depositing 2 g of an Ag–rGO dispersion (1 mg g^{-1}) onto a silicon wafer, followed by drying in a vacuum oven. By a similar method, Ag–rGO can be replaced with Ag or R–rGO to obtain Ag or R–rGO substrates. The substrates were then immersed in a series of R6G solutions with varying concentrations (10^{-3} mol L^{-1}, 10^{-4} mol L^{-1}, 10^{-5} mol L^{-1}, 10^{-6} mol L^{-1}, 10^{-7} mol L^{-1}) for one hour, after which they were air-dried at room temperature in preparation for Raman spectroscopy analysis. To ensure the reliability of the measurements, each sample was tested at six distinct locations, and the final Raman spectrum was derived from the average of these readings. Furthermore, to calculate the SERS enhancement factors, R6G solution with a concentration of 10^{-2} mol L^{-1} was directly applied onto a silicon wafer substrate for Raman spectral analysis.

The calculation method for SERS enhancement factor is as follows:[35]

$$EF = (I_{SERS}/I_{bulk})/(N_{SERS}/N_{bulk}) \quad (4)$$

where I_{SERS} and I_{bulk} represent the characteristic peak intensities of R6G molecules adsorbed on the active substrate (*i.e.* Ag–rGO substrate, Ag substrate, or R–rGO substrate) and silicon wafer substrate, respectively. N_{SERS} and N_{bulk} correspond to the number of R6G molecules effectively excited by the laser beam to obtain the corresponding SERS and normal Raman spectra, respectively. Assuming the effects of the laser spot area, penetration depth, and the solid density of R6G are negligible, the formula for calculating the enhancement factor can be simplified as follows:[36]

$$EF = (I_{SERS}/I_{bulk})/(c_{SERS}/c_{bulk}) \quad (5)$$

where c_{SERS} and c_{bulk} represent the concentration of R6G molecules that can be irradiated by laser on the active substrate surface and normal Raman spectra, respectively.

The maximum intensity deviation (D) of the SERS spectra to the average intensity is as follows:

$$D = \frac{\Delta I}{I} \times 100\% = \frac{I - I_{average}}{I_{average}} \times 100\% \quad (6)$$

where I is the maximum peak intensity and $I_{average}$ is the average peak intensity.

2.7. Instrument and characterization

UV3150 spectrophotometer (Shimadzu, Japan) was employed to monitor the reduction process and to measure the concentration of R6G. Raman spectra of GO, Ag–rGO powders, and R6G molecules of varying concentrations on different substrates were characterized by LabRAM HR Evolution Raman Spectrometer from HORIBA company. During the testing, a continuous-wave laser at 532 nm served as the excitation source, integrated with a CCD imaging system for micro-area testing and analysis on the material surface. The spot diameter is about 3 μm, with a testing range spanning from 50 nm to 2100 nm. The diffraction peak positions and intensities of GO and Ag–rGO powders were performed on a D/max-2200/PC X-ray diffractometer (Rigaku, Japan) utilizing a Cu Ka X-ray beam. The spectra of X-ray photoelectron spectroscopy (XPS) were achieved by ESCALAB 250 (Thermo Fisher Scientific, USA). The structures were observed by Asylum Research MFP-3D-SA Atom force microscope (AFM) operated in the tapping mode and Hitachi H-800 transmission electron microscope (TEM) with an accelerating voltage of 100 kV. The surface area, pore volume, and average pore size of the samples are determined by the N_2 adsorption/desorption isotherms at 77 K using Quantachrome Instruments NOVA Touch lx4 Model.

3 Results and discussion

3.1. Characterization of Ag–rGO

Fig. 1a displays the UV-vis spectra of GO, Ag, and Ag–rGO obtained *via* the *in situ* synchronous reduction coagulation method. GO exhibits absorption peaks at 228 nm and 300 nm, attributed to the π–π* transitions of C–C (sp^2) and the n–π* transitions of

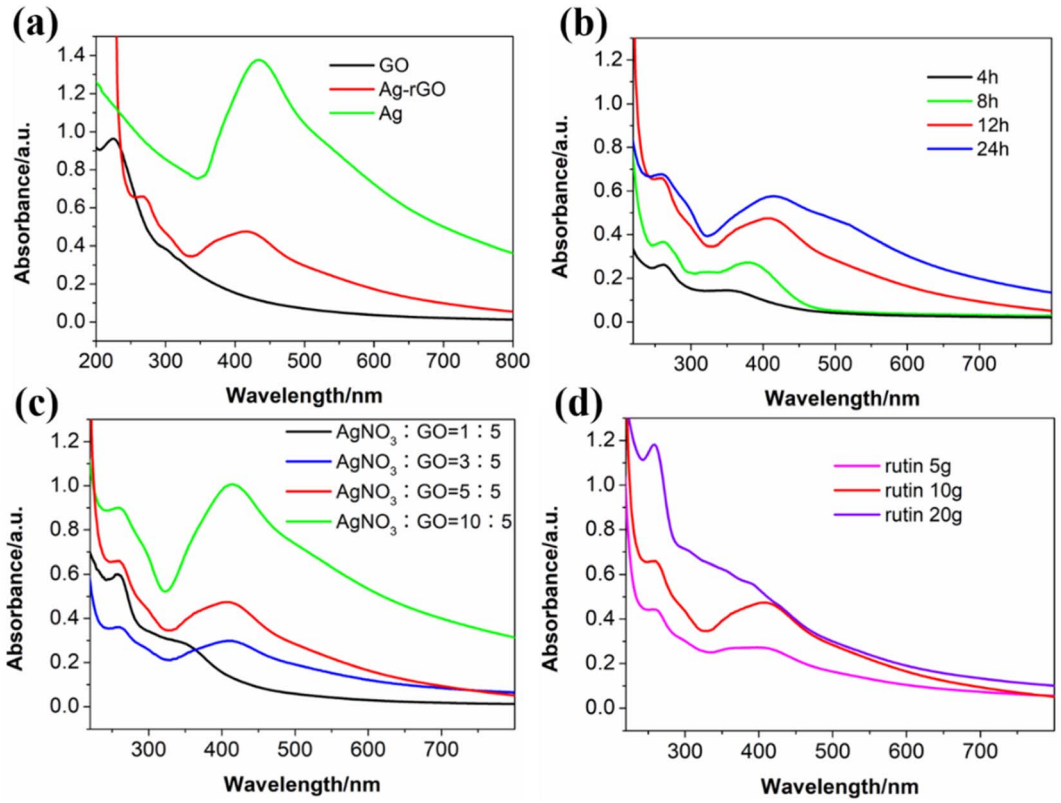

Fig. 1 (a) UV-vis spectra of GO, Ag, and Ag–rGO; (b) UV-vis spectra of Ag–rGO after different reaction times; (c) UV-vis spectra of Ag–rGO obtained by different initial m_{AgNO_3}/m_{GO}; (d) UV-vis spectra of Ag–rGO obtained by using different amounts of rutin.

C–O (sp^3), respectively. The emergence of an absorption peak at 260 nm for Ag–rGO indicates the reduction of GO and the reformation of sp^2 hybridized carbon. The reformation is further corroborated by the analysis of bandgap changes; calculations reveal that the bandgap of GO is 3.82 eV, which is reduced to 3.09 eV for the Ag–rGO sample, confirming the reduction of Ag–rGO.[37] Additionally, Ag–rGO shows an absorption peak around 410 nm, characteristic of Ag's surface plasmon resonance (SPR),[38] suggesting that rutin can also reduce Ag^+ *in situ* to Ag nanoparticles while reducing GO. Generally speaking, an increase in size leads to a decrease in bandgap energy, which causes the absorption peak to shift towards longer wavelengths, that is, a redshift occurs. The SPR peak of pure Ag, located at 430 nm, shows a red shift compared to Ag–rGO, with an increased full width at half maximum and higher intensity, indicating larger Ag nanoparticle sizes and a broader size distribution in the pure Ag, as opposed to those embedded in the Ag–rGO nanocomposite. The reduced size of Ag nanoparticles in Ag–rGO endows the nanocomposite with a larger specific surface area.

To fabricate Ag–rGO free from aggregation, exhibiting excellent water dispersibility, and possessing superior SERS effects and catalytic performance, the experimental conditions, including reaction time, the initial mass ratio of $AgNO_3$ to GO, and the amount of reducing agent, were optimized. Fig. 1b illustrates the UV spectra of Ag–rGO under various reaction times with a fixed mass ratio of 5 : 5 and a reducing agent amount of 10 g. It is observed that no SPR peak for Ag was present when the reaction time was 4 hours; a faint SPR peak emerged when the reaction time reached 8 hours; a more pronounced SPR peak appeared at 410 nm when the reaction time was 12 hours; and a further extension the reaction time to 24 hours resulted in a redshift of the SPR peak (419 nm) and an increase in full width at half maximum, indicating larger Ag nanoparticle sizes and a broadened distribution of Ag nanoparticle sizes. It should be noted that larger Ag nanoparticle sizes are detrimental to the enhancement of the specific surface area, as well as the catalytic and SERS performance of Ag–rGO. Fig. 1c demonstrates the influence of the mass ratio of $AgNO_3$ to GO on the Ag–rGO product. It is noted that no characteristic absorption peak for Ag nanoparticles was observed at a 1 : 5 mass ratio; a clear SPR peak for Ag appeared when the mass ratio was 3 : 5; and at a 5 : 5 ratio, the intensity of the Ag SPR peak further increased, with a full width at half maximum almost identical to that at a 3 : 5 ratio. However, when the mass ratio reaches 10 : 5, the intensity of the Ag SPR peak significantly increased, with a redshift to 424 nm and an increase in full width at half maximum, signaling the aggregation of Ag nanoparticles and the formation of larger-sized Ag nanoparticles. The amount of reducing agent has a significant impact on the degree of reduction, performance, and post-treatment of the product. Therefore, the optimal amount of reducing agent was investigated through experiments 3, 7, and 8 in Table S1.† Fig. 1d presents the UV absorption spectra of the product. It is evident that when the reducing agent dosage is 5 g, the SPR

peak for Ag is not obvious, indicating that insufficient reducing agent leads to poor reduction. When the reducing agent amount is 10 g, it provides an effective reduction for both $AgNO_3$ and GO, whereas the reducing agent amount is 20 g, the characteristic absorption peak for Ag is absent in the UV-vis spectrum, which should be due to the excessive rutin in the system. An excess of rutin not only complicates the post-treatment process but also detracts from the SERS effect and catalytic performance of the product. Therefore, the optimized conditions for the preparation of Ag–rGO are a reaction time of 12 hours, a mass ratio of $AgNO_3$ to GO of 5 : 5, and a reducing agent dosage of 10 g. Unless specified otherwise in this paper, all Ag–rGO were prepared under these optimized conditions.

Under optimized conditions, the Ag–rGO prepared by *in situ* synchronous reduction coagulation method exhibits excellent water dispersibility. The solid powder sample of Ag–rGO can be uniformly dispersed in water under ultrasonic conditions. As evident from the photographs in Fig. S1,† the Ag–rGO aqueous dispersion remains stable even after 5 days of storage, whereas the Ag dispersion shows signs of phase separation. This indicates that Ag–rGO effectively prevents aggregation and enhances the dispersive stability of the product.

Fig. 2a presents the Raman spectra of GO, R–rGO, and Ag–rGO. The D band and the G band are typically observed in GO, R–rGO, and Ag–rGO. The D band located at 1355 cm^{-1} reflects the degree of disorder in the graphite structure, while the G band situated at 1575 cm^{-1} represents the first-order scattering E_{2g} vibrational mode, which is indicative of the sp^2 hybridized carbon structure. Consequently, the intensity ratio (I_D/I_G) can be utilized to analyze the degree of defects or disorder in the sample. As depicted in the figure, GO exhibits a D band at 1347 cm^{-1} and a G band at 1592 cm^{-1}. R–rGO shows a D band at 1345 cm^{-1} and a G band at 1592 cm^{-1}. In Ag–rGO, the D and G bands are observed at 1370 cm^{-1} and 1610 cm^{-1}, respectively. Upon calculation, the I_D/I_G ratio for GO is 0.991, which increases to 1.001 in R–rGO and 1.022 in Ag–rGO. This increase is attributed to the reduction of GO, a process where sp^3 hybridized carbon atoms lose oxygen-containing groups and reform sp^2 hybridized carbon atoms. The newly formed sp^2 regions are isolated from the original sp^2 regions, resulting in a smaller average sp^2 domain in R–rGO and Ag–rGO compared to that in GO. Notably, the I_D/I_G ratio of Ag–rGO exhibited an increase compared to that of R–rGO, suggesting that the loaded silver particles on Ag–rGO exerted a significant enhancement effect on the Raman signal of graphene nanosheets.

Fig. 2b displays the XRD patterns of GO, R–rGO, and Ag–rGO. It is evident from the figure that the diffraction peak of GO (001) is located at $2\theta = 10.0°$. Utilizing Bragg's law, the interlayer spacing of GO is calculated to be 0.88 nm, significantly greater than the reported interlayer spacing of graphite (0.335 nm).[39] This increase in spacing is attributed to the intercalation of oxygen-containing groups, indicating a substantial presence of oxygen-containing groups in GO. The characteristic graphene oxide (GO) diffraction peak disappeared in the R–rGO spectrum, exhibiting instead a broad peak (002) at $2\theta = 23.2°$. This structural transformation arises from a decline in the crystallinity of graphene oxide (GO) and an elevation in structural disorder. In the case of Ag–rGO, the diffraction peak at $2\theta = 10°$ has also completely vanished, suggesting that most of the oxygen-containing functional groups in GO have been reduced. A weaker and broader diffraction peak appears in Ag–rGO, positioned around $2\theta = 21.7°$, which is attributed to the (002) plane of rGO.[28,40] Additionally, Ag–rGO exhibits diffraction peaks at $2\theta =$ 38.2°, 44.2°, 64.6°, 77.4°, and 81.4°, corresponding to the (111), (200), (220), (311), and (222) crystal planes of silver cubic.[41] These peaks confirm the formation of Ag–rGO nanocomposites. Notably, the relative peak intensity of the (111) plane is approximately five times that of the (200) plane, indicating a preferred orientation of Ag–rGO along the (111) plane.

X-ray photoelectron spectroscopy (XPS) analysis was conducted to investigate the chemical composition and oxidation states. The survey spectrum presented in Fig. S2† unambiguously revealed characteristic peaks corresponding to C 1s, O 1s, and Ag 3d in Ag–rGO. In contrast, the survey spectra of GO and R–rGO exclusively displayed characteristic peaks corresponding to C 1s and O 1s. Moreover, Fig. 3a–c depict the C 1s spectra of GO, R–rGO, and Ag–rGO, respectively. It is observable that the C 1s spectrum of GO exhibits peaks at 284.4, 285.2, 287.1, and 288.6 eV, corresponding to C–C (sp^2), C–O (sp^3), C═O, and π–π* transitions.[37] Similar peaks are observed in R–rGO and Ag–

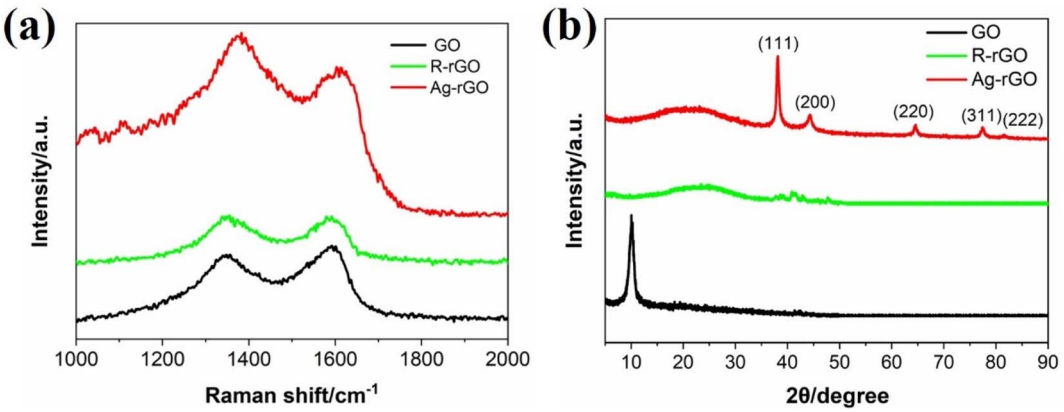

Fig. 2 (a) Raman spectra, (b) XRD spectra of GO, rGO, and Ag–rGO.

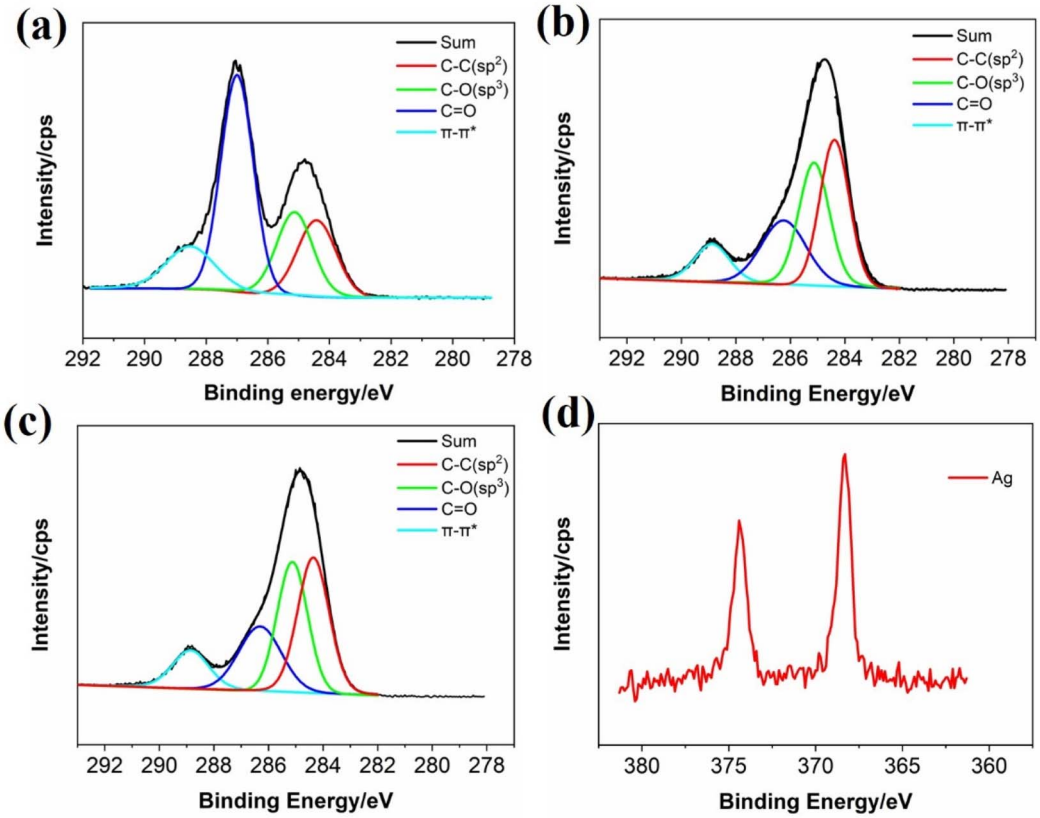

Fig. 3 XPS spectra: (a) C 1s spectra of GO; (b) C 1s spectra of R–rGO; (c) C 1s spectra of Ag–rGO; (d) Ag 3d spectra of Ag–rGO.

rGO, albeit with altered relative intensities. The intensity of the C=O peak in R–rGO and Ag–rGO are significantly diminished, while the intensity of the sp^2 hybridized peak is notably increased, indicating the occurrence of the reduction reaction. The increased intensity of the C–O (sp^3) peak in R–rGO and Ag–rGO are likely related to the formation of C–O bonds following the reduction of C=O. Additionally, the Ag 3d spectrum is detectable in the Ag–rGO sample, as shown in Fig. 3d, where peaks at 368.3 and 374.3 eV correspond to the Ag $3d_{5/2}$ and $3d_{3/2}$, respectively.[42] Based on the semi-quantitative analysis of XPS, the content ratios of O and C elements in the GO, R–rGO, and Ag–rGO, as well as the intensity ratios of each spectral peak, are shown in Table S2.† The data demonstrate enhancement in the C/O ratio from GO to R–rGO or Ag–rGO, indicating the effective removal of oxygen-containing functional groups during the reduction reaction.

Fig. 4 presents the AFM images of GO, R–rGO, and Ag–rGO. The height profile of Ag–rGO reveals a thickness range of about 2 nm to 6 nm. In contrast, the height profile of GO is approximately 1.5 nm, which is smaller than the average thickness of R–rGO and Ag–rGO. In addition, the thickness of R–rGO without Ag loading is approximately 2–3 nm. Consequently, the significant increase in the thickness of Ag–rGO is attributed to the loading of Ag nanoparticles on the graphene surface.

Fig. 5 displays the TEM images of GO, R–rGO, and Ag–rGO at the scale of 100 nm, respectively. GO exhibits a typical transparent crumpled flake structure without any other particles loaded on it. The morphology of R–rGO is similar to that of GO, also exhibiting transparency with a corrugated and lamellar structure. This indicates that R–rGO does not experience agglomeration. However, there is a slight increase in the number of layers and the wrinkles on the sheet, which can be attributed to the reduction reaction.[43] The TEM image of Ag–rGO reveals that Ag is uniformly loaded on the rGO in the form of nanosheets with sizes around 10 nm, with only a small number of Ag particles aggregating and increasing in size. The rGO layers in Ag–rGO also do not aggregate, demonstrating that the composite of Ag and rGO has prevented both the agglomeration of Ag nanoparticles and the stacking of rGO layers. This is because, during the preparation of Ag–rGO, the functional groups and negative charges on the surface of GO facilitated the adsorption of Ag^+ on the GO surface, which in turn promoted the uniform nucleation and growth of Ag nanoparticles on the rGO layers. Through a bidirectional synchronous reduction coagulation process, Ag–rGO nanocomposite with excellent dispersion and no agglomeration was ultimately formed.

3.2. Catalysts reduction of methylene blue

Before studying the catalytic reduction performance, we first investigated the porosity *via* BET, with their N_2 adsorption–desorption isotherms shown in Fig. S3.† The larger specific surface areas and pore structures can provide more favorable conditions for pollutant attachment. This corresponds to

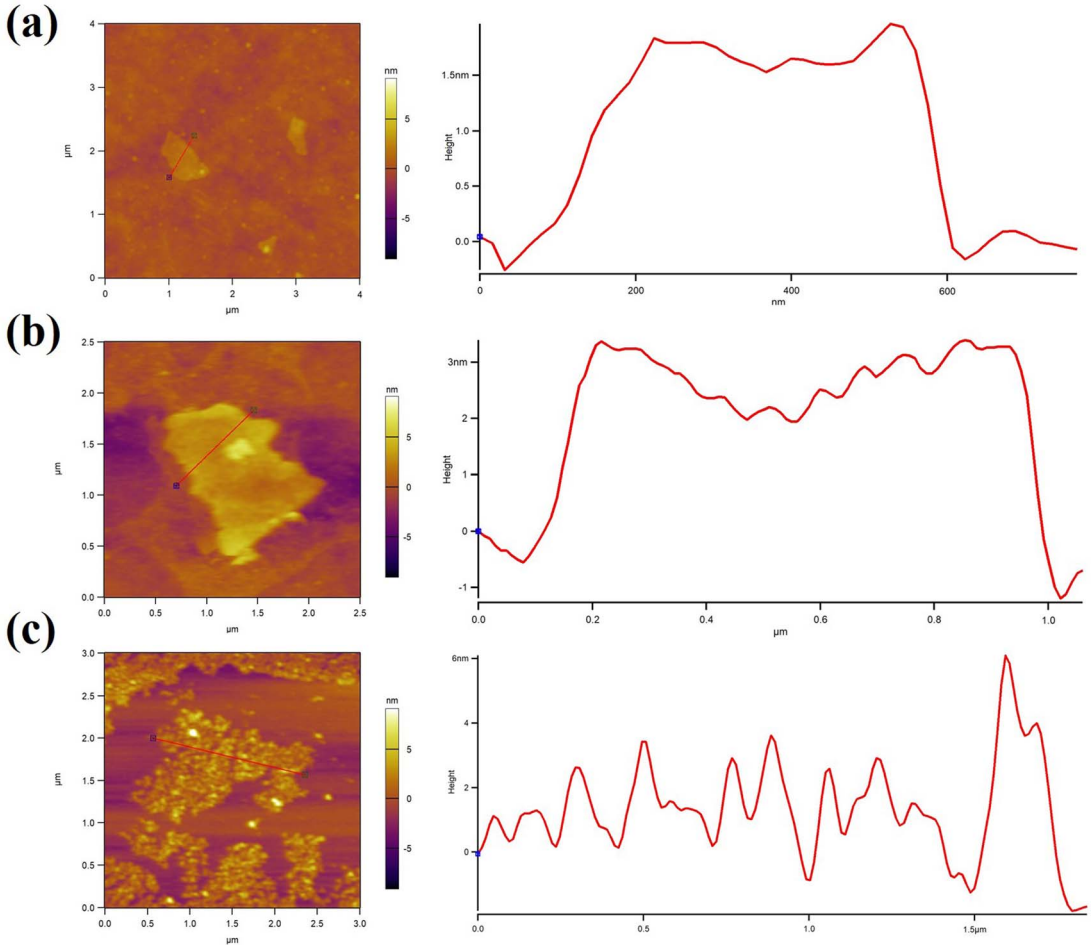

Fig. 4 AFM images of (a) GO, (b) R–rGO, and (c) Ag–rGO.

improved removal efficiencies of the materials for contaminants. The nitrogen adsorption/desorption isotherm curves of GO and Ag–rGO are attributed to type IV as shown in Fig. S3,† which indicates that the samples can be classified to materials with mesopore. Moreover, Table S3† lists the detailed data for the surface area and pore structure of GO and Ag–rGO. This table suggests that Ag–rGO exhibits a BET specific surface area of 35.67 $m^2\ g^{-1}$, and an average pore size of 3.79 nm, significantly higher than that of GO (12.01 $m^2\ g^{-1}$ or 3.10 nm). The enhancement can be attributed to the inherently large specific surface area of nano-Ag. The incorporation of Ag nanoparticles creates conducive structural characteristics, including enhanced surface area and optimized electron transfer pathways, which collectively promote superior catalytic activity.

Methylene blue (MB) is an alkaline phenylamine dye, also known as methylthioninium chloride, which has a wide range of applications in biology, chemistry, dyeing, medicine, and other fields, but is harmful to humans. Removing MB from wastewater is beneficial to the environment and human health. MB appears blue in its oxidized state and becomes colorless upon reduction. Due to $\pi \rightarrow \pi^*$ and $n \rightarrow \pi^*$ transitions, the maximum absorption wavelength (λ_{max}) of an MB aqueous solution is located at 664 nm, and the peak intensity at λ_{max} decreases after the catalytic reduction reaction occurs.

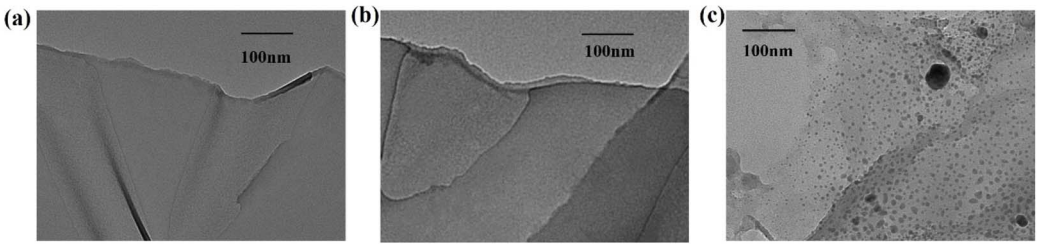

Fig. 5 TEM images of (a) GO, (b) R–rGO and (c) Ag–rGO.

Therefore, the catalytic performance of Ag–rGO-5-5 can also be studied by measuring the rate of change in absorbance at the characteristic absorption wavelength in the UV-vis spectrum during the reduction of MB dye.

The effect of the additional amount of Ag–rGO nanocomposite on the MB reduction reaction is shown in Fig. 6. Fig. 6a–c indicate that after adding Ag–rGO, the intensity of MB's absorption spectrum decreases significantly with the extension of reaction time. As the amount of Ag–rGO added increases from 1 mg (a) to 2 mg (b) and then to 3 mg (c), the rate of decrease in the absorption spectrum intensity also varies, with a larger amount leading to a faster decrease. When the amount of Ag–rGO added is 3 mg and the reaction time is 9 minutes, MB is almost completely reduced, forming colorless leucomethylene blue (LMB), as shown in the inset of Fig. 6c. Fig. 6d presents the relationship between the maximum absorbance of the MB solution and the amount of Ag–rGO added at different reaction times. It is evident that, at the same reaction time, the greater the amount of Ag–rGO added, the lower the absorbance at λ_{max}, indicating a higher reduction efficiency. At a reaction time of 9 minutes, the maximum absorbance of the MB solution with 1, 2, and 3 mg of Ag–rGO added drops to 1.222, 0.609, and 0.149, respectively, with decolorization rates of 70%, 85%, and 96%.

Fig. S4a† illustrates the change of $\ln(c_t/c_0)$ with reaction time t for different addition amounts of Ag–rGO. Here, c_0 represents the initial concentration of the MB solution (100 mg L^{-1}), and c_t is the concentration of the MB solution reduced by $NaBH_4$ for t minute. The catalytic reduction reaction can be observed to conform to a pseudo-first-order kinetic model. Furthermore, the reaction rate constants can be derived from the slopes as shown in Table 1. When the addition amounts are 1 mg, 2 mg, and 3 mg, the reaction rates are 0.129 min^{-1}, 0.162 min^{-1}, and 0.362 min^{-1}, respectively. This is attributed to the fact that an increased content of Ag–rGO leads to a greater number of active sites, which facilitates electron transfer during the reduction process.

Fig. S4b† presents the UV-vis spectrum of MB reduced by $NaBH_4$ for 30 minutes without the addition of Ag–rGO. It can be observed that when $NaBH_4$ is stirred with MB at room temperature for 30 minutes, the decolorization rate of MB reaches 32%. In contrast, as mentioned earlier, with the addition of 1 mg Ag–rGO, the MB solution achieves a decolorization rate of 70% after being reduced for only 9 minutes. This indicates that Ag–rGO can significantly accelerate the rate of the MB reduction reaction, demonstrating its efficiency as a catalyst.

Table 1 The reaction rates and correlation coefficients of MB in the presence of Ag–rGO

Ag–rGO amount/mg	K/min^{-1}	R^2	Time/min
1	0.129	0.991	15
2	0.162	0.973	15
3	0.362	0.987	9

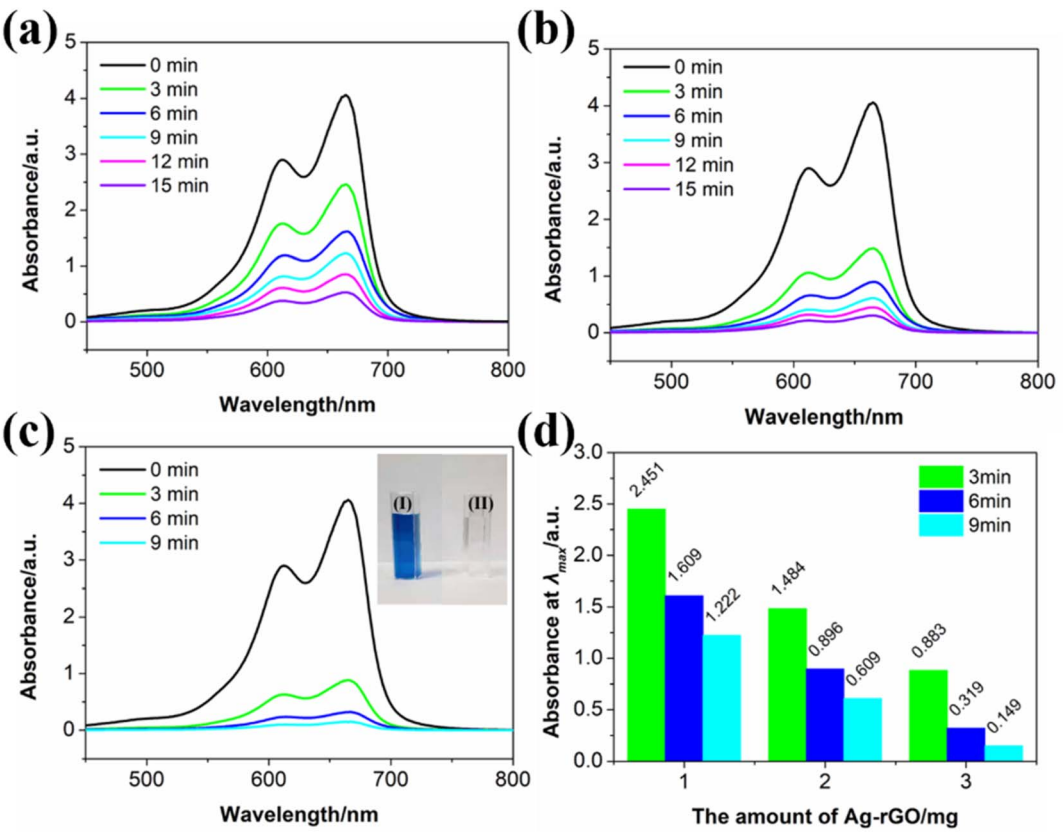

Fig. 6 UV-vis spectra of MB solution reduced by $NaBH_4$ when the addition amount of Ag–rGO is (a) 1 mg, (b) 2 mg, and (c) 3 mg; (d) variation of absorbance at λ_{max} depending on time and addition amount.

Additionally, we investigate the adsorption effect of Ag–rGO nanocomposite on MB in the absence of $NaBH_4$, as depicted in Fig. S4c.† After the addition of Ag–rGO for 30 minutes, the decolorization rate of MB is 40%. Therefore, we conclude that both adsorption and catalytic reduction can promote the degradation of MB. The adsorption capacity of Ag–rGO for MB allows more MB molecules to come into contact with the catalyst, thereby facilitating the reduction reaction.

Fig. S4d† presents the UV-vis spectrum of MB after being reduced by $NaBH_4$ for 30 minutes in the presence of 3 mg Ag. It is observable from the spectrum that Ag alone possesses catalytic activity, achieving a decolorization rate of 62% for MB after a reaction time of 30 minutes. However, with the addition of an equivalent mass of Ag–rGO, the decolorization rate of MB reaches 96% within just 9 minutes, indicating that the catalytic reduction effect of Ag–rGO is much superior to that of Ag alone. This enhancement is attributed to the *in situ* synchronous reduction coagulation method used to prepare Ag–rGO under optimized conditions, where graphene inhibits the aggregation of Ag nanoparticles through nucleation and anchoring effects. Consequently, the size of Ag nanoparticles in Ag–rGO is reduced, endowing the composite with a larger surface area, which is conducive to improving catalytic performance. Additionally, the *in situ* enrichment effect of the composite (capable of adsorbing a substantial amount of MB, providing a higher concentration of dye molecules near the catalyst) and its superior electron transfer efficiency (during the reaction between MB dye and $NaBH_4$, electron transfer occurs. $NaBH_4$ acts as an electron donor, and MB as an electron acceptor. Ag–rGO can serve as an electron transfer intermediary between MB dye and BH_4^-, reducing bond dissociation energy at the onset of the reaction) and also contributing to the heightened catalytic activity of Ag–rGO.

In addition to catalytic activity, the stability of the catalyst is another crucial factor for practical applications. The stability of Ag and Ag–rGO was evaluated over six reaction cycles, with the decolorization rates depicted in Fig. S5.† After each cycle, the degradation rate of Ag experienced a significant drop, decreasing from 62% to 39%. In contrast, Ag–rGO only saw a minor decrease in its degradation rate, which still hovered at 89% even after the sixth cycle. The results demonstrate the superior catalytic stability of Ag–rGO. As such, Ag–rGO stands out as a remarkably efficient and stable catalyst for the degradation of organic dyes within water purification systems.

3.3. SERS activity of Ag–rGO

SERS is a non-destructive and highly sensitive analytical technique with broad application prospects in the monitoring of environmental pollutants, chemical detection, explosive detection, and biosensing. Rhodamine 6G (R6G), also known as Rose Bengal, is a catechol-based fluorescent dye widely used in agriculture, dyes, fragrances, rubber, medicine, and photosensitive materials, and is commonly employed as a probe molecule for studying the SERS effect.

Fig. 7a illustrates the Raman spectra of R6G solutions at a concentration of 10^{-4} mol L^{-1} using Ag–rGO-3-5, Ag–rGO-5-5,

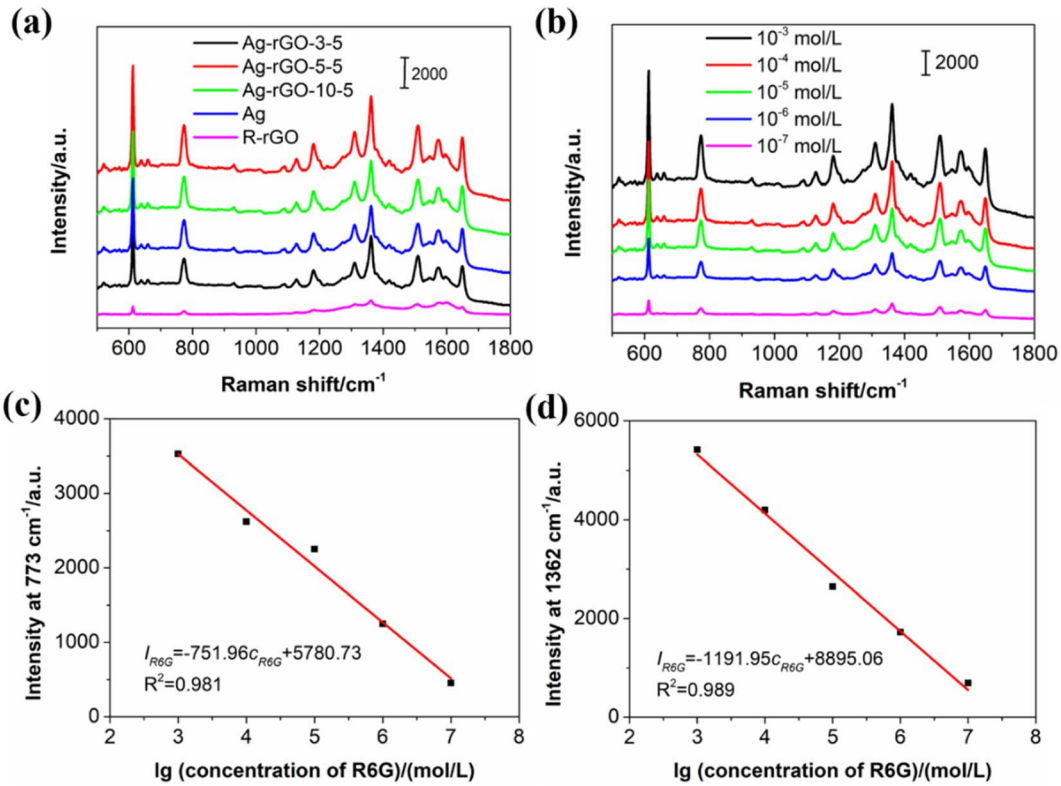

Fig. 7 (a) Raman spectra of R6G solution (10^{-4} mol L^{-1}) on different substrates; (b) Raman spectra of R6G solution with different concentration on Ag–rGO substrate; variation of the Raman intensity at (c) 773 cm^{-1} and (d) 1362 cm^{-1} as the function of R6G solution concentration.

Ag–rGO-10-5, Ag, and R–rGO as substrates. Characteristic peaks of R6G can be observed at 614 cm^{-1}, 773 cm^{-1}, and 1183 cm^{-1}, corresponding to the inter-ring bending vibrations of C=C–C, out-of-plane deformation vibration of the C–H group, and in-plane bending motions of C–H bonds, respectively; the peaks at 1310 cm^{-1}, 1362 cm^{-1}, 1509 cm^{-1}, and 1650 cm^{-1} are attributed to the stretching vibrations of aromatic C–C bonds.[44] Furthermore, comparing the SERS effects of various substrates reveals that R–rGO can produce a certain SERS effect, with an enhancement factor (EF) of 38 at the 773 cm^{-1} peak, due to the chemical enhancement effect, fluorescence quenching of the molecule, and high adsorption capacity for target molecules. The Ag substrate exhibits the typical electromagnetic enhancement effect of noble metals, which is higher than the chemical enhancement, hence the Raman spectral intensity of R6G on the Ag substrate is higher than that on the R–rGO substrate. The substrates Ag–rGO-3-5, Ag–rGO-5-5, and Ag–rGO-10-5, which possess both chemical and electromagnetic enhancement effects, all exhibit excellent SERS effects, with the highest intensity for Ag–rGO-5-5. This is because Ag–rGO-3-5 has fewer Ag nanoparticles with larger interparticle distances, resulting in weaker localized surface plasmon resonance and insufficient "hot spots"; in Ag–rGO-10-10, the higher initial amount of Ag^{+} leads to more Ag crystal nuclei and nanoparticles, which are prone to agglomeration; whereas Ag–rGO-5-5, in addition to combining chemical and electromagnetic enhancement effects, also has good dispersion stability and can inhibit the aggregation of Ag nanoparticles. The results indicate that the relative content and agglomeration degree of Ag nanoparticles in Ag–rGO nanocomposites significantly affect their SERS performance.

Fig. 7b shows the Raman spectra of R6G probe molecules at different concentrations using Ag–rGO as the substrate. It can be observed that the Raman spectral intensity of the R6G solution is directly proportional to its concentration, decreasing as the concentration of the R6G solution drops from 10^{-3} mol L^{-1} to 10^{-7} mol L^{-1}. Even at a concentration of 10^{-7} mol L^{-1}, the characteristic peaks of R6G are still observable, indicating that the detection limit for R6G molecules using Ag–rGO is 10^{-7} mol L^{-1}. The EF at the 773 cm^{-1} peak is calculated to be 3.03×10^{5}. These results demonstrate that the Ag–rGO substrate has the advantages of a high signal-to-noise ratio, high sensitivity, and low detection limit.

Fig. 7c and d display the relationship between the Raman spectral intensity at 773 cm^{-1} and 1362 cm^{-1} of the R6G probe molecules and their concentration using Ag–rGO as the substrate. As the concentration of the R6G solution increases, the Raman spectral intensity increases and there is an approximate linear correlation between them. Fitting the concentration and intensity in the form of $I_{R6G} = ac_{R6G} + b$, the linear relationships at 773 cm^{-1} and 1362 cm^{-1} are obtained as $I_{R6G} = -751.96c_{R6G} + 5780.73$, and $I_{R6G} = -1191.95c_{R6G} + 8895.06I_{R6G}$, with correlation coefficients of 0.981 and 0.999, respectively, indicating good correlation and suggesting that the Ag–rGO substrate can be used to predict the concentration of probe molecules.

To investigate the differences in stability between Ag–rGO and Ag substrates, both substrates, spotted with a 10^{-4} mol L^{-1}

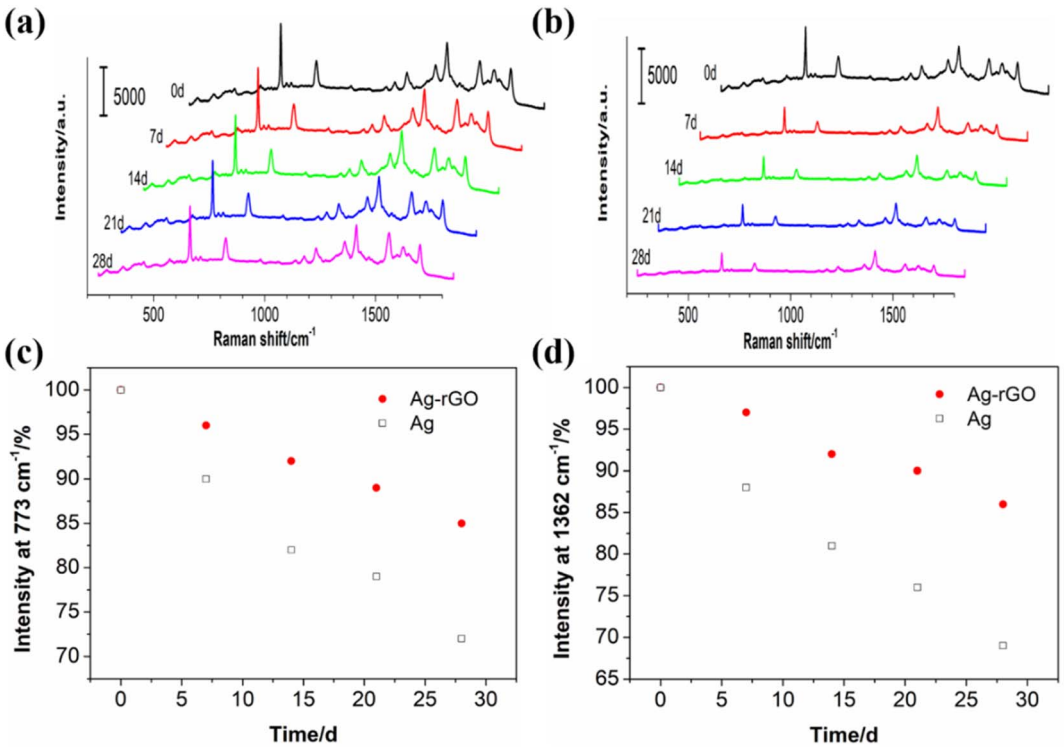

Fig. 8 Raman spectra of R6G on (a) Ag–rGO substrate and (b) Ag substrate exposed for 0–28 days; The percentage variation of Raman signal intensity at (c) 773 cm^{-1} and (d) 1362 cm^{-1} as the function of exposure time.

Table 2 Comparative table for different catalyst studies based on k and SERS substrate studies based on enhancement factor (EF) and limit of detection (LOD)

	Catalytic activity for MB			SERS performance for R6G		
Samples	Catalyst mass	Time	k	EF	LOD	Ref.
Fe_3O_4@C–TiO_2–Ag	10 mg	600 s	0.0063 s^{-1}	—	—	45
Ce–BiOBr/Bi_2S_3	10 mg	12 min	0.170 min^{-1}	—	—	46
AgNPS-MCM-41	3 mg	420 s	0.0048 s^{-1}	—	—	47
CuPMoV	39.8 mg	90 s	0.0246 s^{-1}	—	—	48
Fe_3O_4@AC	7 mg	12.5 min	0.34 min^{-1}	—	—	49
Ag–NiO	—	—	—	2.89×10^4	10^{-5} M	50
ZnO	—	—	—	6.1×10^5	10^{-7} M	51
Au-coated sinusoidal	—	—	—	—	10^{-5} M	52
Fe_3O_4@SiO_2@Ag	—	—	—	1.34×10^5	10^{-7} M	53
Ag–rGO	3 mg	3 min	0.362 min^{-1}	3.03×10^5	10^{-7} M	This study

R6G probe solution, were subjected to Raman spectroscopy testing after 0, 7, 14, 21, and 28 days of storage. The corresponding results are displayed in Fig. 8a and b. It is evident from the figures that the Raman spectral intensity of the R6G probe molecules on both Ag–rGO and Ag substrates decreases with extended storage time, with the Ag substrate showing a more pronounced reduction in spectral intensity. Fig. 8c and d illustrate the variation in the characteristic peak intensities of the R6G Raman spectra at 773 cm^{-1} and 1362 cm^{-1} on the two substrates over time. It can be observed that the rate of decline differs between the Ag–rGO and Ag substrates. For the Ag–rGO substrate, after 7 and 28 days of storage, the Raman spectral intensity at 773 cm^{-1} drops to 96.12% and 85.06% of the initial value, and at 1362 cm^{-1} it decreases to 97.09% and 86.37%. In contrast, for the Ag substrate, the Raman spectral intensity at 773 cm^{-1} decreases to 90.23% and 72.11% of the initial value after 7 and 28 days, respectively, and at 1362 cm^{-1} it drops to 88.23% and 69.02%. This disparity is attributed to the protective (antioxidant) effect of rGO on the metal in Ag–rGO, which results in a slower oxidation rate for the Ag–rGO substrate compared to the Ag substrate.

In addition to high stability, another key issue is achieving highly reproducible SERS signals over a millimeter-scale range on the same substrate, or even on different SERS substrates. The SERS spectra of R6G molecules at a concentration of 10^{-4} mol L^{-1} were obtained from 20 distinct positions within the same Ag–rGO or Ag substrates, or obtained from different Ag–rGO or Ag substrates, and the corresponding results are shown in Table S4.† As depicted in Table S4,† from different positions on the same substrate, the maximum intensity deviation (D) of the SERS spectra of Ag–rGO shows a minor fluctuation in the range of 4.95% to 7.01%, compared with the range of 7.34% to 9.65% on Ag substrate is smaller, which is attributed to the graphene layer, which captures target molecules effectively through its delocalized π-bonds, thereby reducing signal fluctuations. Additionally, the graphene layer effectively quenches background fluorescence, further enhancing spectral stability. There is a slightly larger D from different Ag–rGO and Ag substrates as shown in Table S4,† however, the D fluctuations of the Ag–rGO are still smaller than that of the Ag substrate, which indicates the Ag–rGO substrate exhibits superior reproducibility.

Finally, we conducted a comparative analysis of the performance parameters of similar recent studies, as illustrated in Table 2. The table demonstrates that the Ag/rGO composite prepared *via* our facile and green one-step exhibits both outstanding catalytic performance and excellent Surface-Enhanced Raman Scattering (SERS) performance.

4 Conclusion

In this work, Ag–rGO nanocomposites were successfully synthesized using graphene oxide (GO) as both the carrier and template, silver nitrate ($AgNO_3$) as the precursor and rutin functioning dually as the reducing and stabilizing agent through the application of the *in situ* synchronous reduction and coagulation method. Characterization *via* X-ray photoelectron spectroscopy (XPS), transmission electron microscopy (TEM), and atomic force microscopy (AFM) revealed that Ag nanoparticles, approximately 10 nm in size, are stably anchored onto partially reduced graphene oxide nanosheets, resulting in a composite with excellent dispersibility in water. In contrast, standalone Ag nanoparticles exhibited larger sizes and inferior water dispersibility. UV-vis spectroscopy was utilized to investigate the effects of the initial mass ratio of $AgNO_3$ to GO, reduction time, and the amount of reducing agent on the prepared Ag–rGO. It was found that when the mass ratio is 1, the reduction time is 12 hours, and the reducing agent amount is 10 g, Ag nanoparticles are well-dispersed on the graphene sheets without aggregation. The prepared Ag–rGO was tested as the SERS substrate and a catalyst. The results demonstrated that the Ag–rGO (3 mg) displayed a corresponding reaction rate constant (k) of 0.362 min^{-1} for the reduction of methylene blue (MB), which can be ascribed to its *in situ* enrichment capability and superior electron transfer efficiency. Furthermore, the Ag–rGO substrate exhibits an excellent SERS effect in terms of detection limits in the order of 10^{-7} M R6G, enhancement factor (3.03×10^5), and high reproducibility (the maximum intensity deviation < 7.01%), attributed to the synergistic combination of Ag's typical electromagnetic enhancement,

graphene's chemical enhancement, the quenching of molecular fluorescence, and its exceptional adsorption capacity for target molecules. Meanwhile, this work provides a facile and general one-step approach for modifying metal nanoparticles on the surface of rGO, enabling their application as both nanocatalysts and SERS substrates.

Data availability

The authors confirm that the data supporting the findings of this study are available within the article.

Conflicts of interest

The authors declare no conflict of interest.

Acknowledgements

This work was supported by the Jiaxing Science and Technology Plan Project (Grant No. 2023AY11023).

References

1 R. Al-Tohamy, S. S. Ali, F. Li, K. M. Okasha, Y. A. G. Mahmoud, T. Elsamahy, H. Jiao, Y. Fu and J. Sun, *Ecotoxicol. Environ. Saf.*, 2022, **231**, 113160.
2 M. Thakur, A. Singh, A. Dubey, A. K. Sundramoorthy, P. Kumar and S. Arya, *Emergent Mater.*, 2024, **7**, 1805–1817.
3 A. Mary Ealias, G. Meda and K. Tanzil, *Rev. Environ. Contam. Toxicol.*, 2024, **262**, 16.
4 V. Katheresan, J. Kansedo and S. Y. Lau, *J. Environ. Chem. Eng.*, 2018, **6**, 4676–4697.
5 G. T. Tee, X. Y. Gok and W. F. Yong, *Environ. Res.*, 2022, **212**, 113248.
6 S. Balu, D. Ganapathy, S. Arya, R. Atchudan and A. K. Sundramoorthy, *RSC Adv.*, 2024, **14**, 14392–14424.
7 A. Haleem, A. Shafiq, S.-Q. Chen and M. Nazar, *Molecules*, 2023, **28**, 1081.
8 M. A. Semião, C. W. I. Haminiuk and G. M. Maciel, *J. Environ. Chem. Eng.*, 2020, **8**, 103617.
9 S. Kutluay and F. Temel, *Colloids Surf., A*, 2021, **609**, 125848.
10 M. M. Hassan and C. M. Carr, *Chemosphere*, 2018, **209**, 201–219.
11 Y. Situ, C. Huang, Y. Yang, Z. Liao and X. Mao, *Environ. Technol. Innovation*, 2023, **32**, 103371.
12 A. V. Baskar, N. Bolan, S. A. Hoang, P. Sooriyakumar, M. Kumar, L. Singh, T. Jasemizad, L. P. Padhye, G. Singh, A. Vinu, B. Sarkar, M. B. Kirkham, J. Rinklebe, S. Wang, H. Wang, R. Balasubramanian and K. H. M. Siddique, *Sci. Total Environ.*, 2022, **822**, 153555.
13 A. Anderson, A. Anbarasu, R. R. Pasupuleti, S. Manigandan, T. Praveenkumar and J. A. Kumar, *Chemosphere*, 2022, **295**, 133724.
14 D. Bekchanov, M. Mukhamediev, S. Yarmanov, P. Lieberzeit and A. Mujahid, *Carbohydr. Polym.*, 2024, **323**, 121397.
15 H. A. Asmaly, B. Abussaud, Ihsanullah, T. A. Saleh, A. A. Bukhari, T. Laoui, A. M. Shemsi, V. K. Gupta and M. A. Atieh, *Toxicol. Environ. Chem.*, 2015, **97**, 1164–1179.
16 A. Dubey, A. Ahmed, A. Singh, A. K. Sundramoorthy and S. Arya, *Diamond Relat. Mater.*, 2024, **149**, 111596.
17 A. Dubey, A. Singh, A. Ahmed, A. K. Sundramoorthy, S. P. Patole and S. Arya, *Surf. Interfaces*, 2024, **51**, 104731.
18 M. Franzreb, *Curr. Opin. Colloid Interface Sci.*, 2020, **46**, 65–76.
19 O. Bunkoed, N. Orachorn, S. Jullakan and P. Nurerk, *TrAC, Trends Anal. Chem.*, 2024, **177**, 117808.
20 M. Saidul Islam Ropak, F. Yasmin, M. A. Rahaman and U. Salma, *Colloids Surf., A*, 2025, **704**, 135477.
21 X. Zhang, W. Li, X. Wang, M. Su and Q. Lin, *J. Mol. Liq.*, 2024, **411**, 125753.
22 Y. Lin, Y. Cao, Q. Yao, O. J. H. Chai and J. Xie, *Ind. Eng. Chem. Res.*, 2020, **59**, 20561–20581.
23 C. Xiao, B.-A. Lu, P. Xue, N. Tian, Z.-Y. Zhou, X. Lin, W.-F. Lin and S.-G. Sun, *Joule*, 2020, **4**, 2562–2598.
24 A. N. Nabeel and A. Jain, in *Electrocatalytic Materials*, ed. S. Patra, S. K. Shukla and M. Sillanpää, Springer Nature Switzerland, Cham, 2024, pp. 67–108, DOI: **10.1007/978-3-031-65902-7_3**.
25 Y. Wang, J. Mao, X. Meng, L. Yu, D. Deng and X. Bao, *Chem. Rev.*, 2019, **119**, 1806–1854.
26 A. Dubey, A. Singh, A. K. Sundramoorthy, S. Dixit, N. I. Vatin and S. Arya, *J. Environ. Chem. Eng.*, 2025, **13**, 115155.
27 M. Li, L. Huang, X. Wang, Z. Song, W. Zhao, Y. Wang and J. Liu, *J. Colloid Interface Sci.*, 2018, **529**, 444–451.
28 C. Yang, Y. Yu, Y. Xie, D. Zhang, P. Zeng, Y. Dong, B. Yang, R. Liang, Q. Ou and S. Zhang, *Appl. Surf. Sci.*, 2019, **473**, 83–90.
29 J. Ahmad and K. Majid, *Adv. Compos. Hybrid Mater.*, 2018, **1**, 374–388.
30 K. Hareesh, R. P. Joshi, S. S. Dahiwale, V. N. Bhoraskar and S. D. Dhole, *Mater. Lett.*, 2016, **164**, 35–38.
31 L. Yang, J.-H. Lee, C. Rathnam, Y. Hou, J.-W. Choi and K.-B. Lee, *Nano Lett.*, 2019, **19**, 8138–8148.
32 C. Lan, J. Zhao, L. Zhang, C. Wen, Y. Huang and S. Zhao, *RSC Adv.*, 2017, **7**, 18658–18667.
33 Y. Jia, T. Qiu, L. Guo, J. Ye, L. He and X. Li, *ACS Appl. Nano Mater.*, 2018, **1**, 1541–1550.
34 J. Tauc, *Mater. Res. Bull.*, 1968, **3**, 37–46.
35 Q. Huang, J. Wang, W. Wei, Q. Yan, C. Wu and X. Zhu, *J. Hazard. Mater.*, 2015, **283**, 123–130.
36 D. C. Rodrigues, M. L. de Souza, K. S. Souza, D. P. dos Santos, G. F. S. Andrade and M. L. A. Temperini, *Phys. Chem. Chem. Phys.*, 2015, **17**, 21294–21301.
37 A. Jilani, M. H. D. Othman, M. O. Ansari, R. Kumar, A. Alshahrie, A. F. Ismail, I. U. Khan, V. K. Sajith and M. A. Barakat, *New J. Chem.*, 2017, **41**, 14217–14227.
38 S. Basiri, A. Mehdinia and A. Jabbari, *Sens. Actuators, B*, 2018, **262**, 499–507.
39 I. K. Moon, J. Lee, R. S. Ruoff and H. Lee, *Nat. Commun.*, 2010, **1**, 73.
40 Y. Niu and R. Xing, *Mater. Chem. Phys.*, 2025, **335**, 130531.

41 J. Junaidi, L. Afrilaini, P. Manurung, S. Sembiring, K. Triyana and S. Hadi, *J. Nano Res.*, 2022, **71**, 1–12.
42 H. Zhao, H. Fu, T. Zhao, L. Wang and T. Tan, *J. Colloid Interface Sci.*, 2012, **375**, 30–34.
43 Y. Lei, Z. Tang, R. Liao and B. Guo, *Green Chem.*, 2011, **13**, 1655–1658.
44 T. K. Naqvi, A. K. Srivastava, M. M. Kulkarni, A. M. Siddiqui and P. K. Dwivedi, *Appl. Surf. Sci.*, 2019, **478**, 887–895.
45 A. N. Chishti, Z. Ma, Y. Liu, M. Chen, J. Gautam, F. Guo, L. Ni and G. Diao, *Colloids Surf., A*, 2021, **631**, 127694.
46 M. T. Mosisa, P. Zhang, B. Wu, L. Chen, Z. Su, P. Li, H. Zhang, A. Farooq, T. Huang, A. B. Abdeta, O. A. Zelekew, D.-H. Kuo, J. Lin, X. Chen and D. Lu, *J. Environ. Chem. Eng.*, 2024, **12**, 113383.
47 B. Asli, S. Abdelkrim, M. Zahraoui, A. Mokhtar, M. Hachemaoui, F. Bennabi, A. B. Ahmed, A. Sardi and B. Boukoussa, *Silicon*, 2022, **14**, 12587–12598.
48 F. Jiang, L.-Y. Kong, J.-Y. Long, B.-L. Fei and X. Mei, *Solid State Sci.*, 2024, **149**, 107453.
49 F. Chergui, A. Mokhtar, S. Abdelkrim, A. Sardi, M. Hachemaoui, B. Boukoussa, A. Djelad, M. Sassi, G. Viscusi and M. Abboud, *Mater. Chem. Phys.*, 2025, **329**, 130094.
50 H. Wu, X. Sun, C. Hou, J. Hou and Y. Lei, *Sensors*, 2018, **18**, 2862.
51 T. Thu Trang, *VNU J. Sci. Math. Phys.*, 2024, **40**, 95–104.
52 N. S. Aminah, T. Lertvanithphol, A. Sathukarn, M. Horprathum, H. Alatas, V. Fauzia, S. P. Santosa, H. Isnaeni, A. Alni and M. Djamal, *Opt. Mater.*, 2024, **149**, 114952.
53 L. Wang, S. Guo, N. Li and M. Wang, *Opt. Commun.*, 2024, **572**, 130954.